LARGE MESH REFLECTORS WITH IMPROVED PATTERN PERFORMANCES

C. Cappellin [(1)], J. R. de Lasson[(1)], R. Jørgensen[(1)], L. Datashvili[(2)], J. Pauw[(2)], N. Maghaldadze[(2)], M. Migliorelli[(3)], J. C. Angevain[(4)]

[(1)] TICRA, Landemærket 29, 1129 Copenhagen, Denmark: cc@ticra.com
[(2)] LSS GmbH, Römerhofweg 51c, 85748 Garching, Germany: leri.datashvili@largespace.de
[(3)] Space Engineering, Via dei Berio, 91, 00155 Roma, Italien Rome, Italy: marzia.miglioelli@space.it
[(4)] ESA/STEC, Keplerlaan 1, 2201 AZ Noordwijk, The Netherlands: Jean.Christophe.Angevain@esa.int

ABSTRACT

This paper focuses on a comparison of possible techniques for grating lobes reduction, applicable to large deployable mesh reflectors based on a peripheral deployable ring. The techniques are applied to the same antenna configuration, and consider not only the theoretical positions of the tensioned net nodes, but also their realistic positions satisfying the condition of force equilibrium in the deployed configuration.

1. INTRODUCTION

Reflectors made by a peripheral deployable ring and a cable network supporting a tensioned net covered by a RF reflective mesh, as shown in Figure 1, are one of the most promising technologies for large deployable reflectors (LDR) in Europe, see [1] and [3].

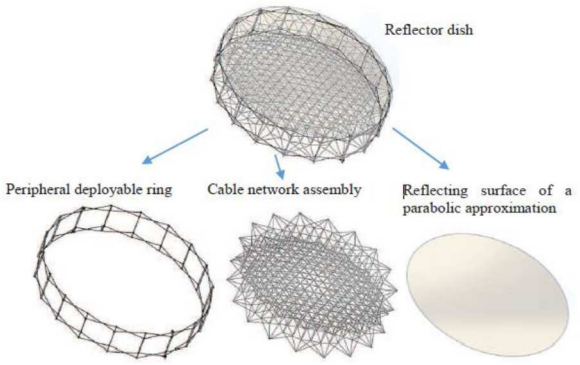

Figure 1. Building blocks of a LDR with peripheral ring technology.

This type of spaceborne reflectors has an excellent potential for Telecommunication and Earth Observation applications in the aperture diameter range of 4-30 meter, due to a high scalability. Moreover, the deployable ring load-bearing structure [1]-[2] and the network assembly of the RF surface recently developed by LSS within the ESA TRP project SCALABLE with HPS [9], see Figure 2, maintain the same size in both deployed and stowed configurations, and are thus more advantageous than the existing ring based reflector flight models, see for example [4] and [5]. These take almost double height in the stowed configuration as compared to the deployed one, see [1].

LDR based on the above technology present however two main limitations. The first one is the periodicity of the tensioned net that supports the RF reflective mesh. The tensioned net is made by cables combining planar triangular facets, whose periodicity causes the generation of grating lobes at angles and with a peak that depend on the frequency of operation and the size of the facets. For a given frequency, the larger is the size of the facets the higher are the grating lobes and the smaller is their angular distance to the main beam. A small facet size reduces the peak of the grating lobes and move them away from the main beam, but may add significant complexity to the cable network. These grating lobes seriously affect telecommunication missions in LEO and GEO orbit (e.g. co-channel interference performance for broadband and multi-beam missions, and co-polarization isolation for broadcast missions). They also seriously affect the signal received by a radiometer antenna sensing the Earth.

Figure 2**.** Double shifted Pantograph ring based crossed network technology demonstrator, ESA project SCALABLE, [9].

The second limitation is that the cable network can currently only produce concave surfaces. This means that LDR can, up to now, produce a contoured beam only when combined with a feed array.

The ESA TRP activity “Advance Techniques for Mesh Reflector with Improved Radiation Pattern Performance”, currently ongoing and contracted to LSS with TICRA and Space Engineering (ESA contract

4000114940/15/NL/MH), has the purpose to investigate techniques to improve the radiation pattern of LDR by tackling the abovementioned limits.

This paper focuses on the first weakness of LDR, namely the generation of grating lobes, and on their reduction through techniques, which introduce a non-regular arrangement of the triangular facets. The techniques are compared and applied to the same antenna configuration, and consider not only the theoretical positions of the tensioned net nodes, but also their realistic positions satisfying the equilibrium of forces in the deployed configuration. More specifically, Section 2 describes the antenna geometry under study, and Section 3 shows the pattern results for the nominal paraboloid and the uniform mesh, which provide, respectively, the best and worst grating lobe performance. In Section 4, three different techniques for grating lobes reduction are presented, and in Section 5 the results of a uniform mesh satisfying the equilibrium of forces are shown. A detailed comparison of all results is given in Section 6 while conclusions are drawn in Section 7.

2. ANTENNA GEOMETRY

The reflector antenna used throughout this paper is illustrated in Figure 3. It is an offset paraboloid with circular projected aperture of diameter D = 12 m, and f/D = 0.7, with f being the focal length of the reflector. The clearance d' is 1.5 m. The feed is pointing towards the centre of the reflector and the edge taper is 12 dB. The feed is polarised in the plane of symmetry and the frequency is selected equal to 1.4 GHz (L-band). In Figure 3 the relevant coordinate systems (CS) are shown: the global CS is the coordinate system in which the paraboloid is defined, where red stays for the x-, green for the y- and blue for the z-axis. The z-axis coincides with the antenna boresight direction.

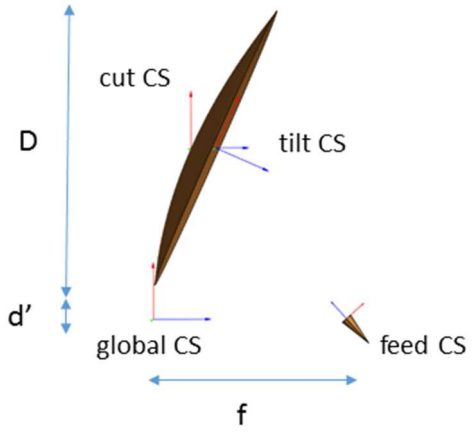

Figure 3. Nominal reflector antenna design, with projected aperture diameter D = 12 m, f = 0.7 and a clearance of 1.5 m. The coordinate systems used in the paper are shown.

The cut CS is parallel to the global CS and has origin at the center of the paraboloid. It is the CS in which all far-field patterns are computed. In the second part of the paper, an additional coordinate system will be used: it is shown in Figure 3 and called tilt CS. Its origin is at the center of the ellipse drawn by the rim of the reflector, and its z-axis is normal to the plane in which the rim is contained. The minor axis of the ellipse is 6 m, while the major axis of the ellipse is 6.57 m. The tilt between the two z-axis of the cut and tilt CS is 24.06°.

3. NOMINAL PARABOLOID AND UNIFORM MESH

A parabolic reflector with a feed at focus generates a constant aperture phase yielding the best possible performance. The nominal paraboloid can conceptually be thought as a mesh reflector with triangular mesh side length s tending to zero. When the paraboloid is generated by a mesh of planar triangular facets, the ideal situation is distorted due to the facets leading to a reduction of the peak directivity. A second, and more visible effect, is the generation of grating lobes. These grating lobes appear at well-defined angular directions, when the size s of the triangular facets is uniform over the reflector. In particular, grating lobes appear at an angle θ_g given by

$$\sin\theta_g = \frac{2\lambda}{s} \tag{1}$$

in the $\varphi = 0° + p\ 60°$ planes and by

$$\sin\theta_g = \frac{2\lambda}{\sqrt{3}s} \tag{2}$$

in the $\varphi = 30° + p\ 60°$ planes, with λ being the wavelength. The far-field pattern in an azimuth and elevation grid given by a uniform mesh with s = 1250 mm can be seen in Figure 4. The grating lobes are clearly visible and show up at the predicted angular directions.

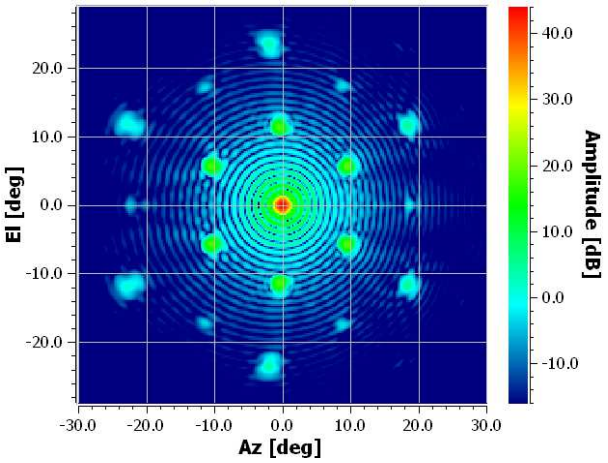

Figure 4. Co-polar radiation pattern for uniform mesh with side length s = 1250 mm.

A cut through the azimuth=0°, or equivalently in the φ=90° cut, is shown in Figure 5 in blue, together with the field of the nominal paraboloid in red. The first grating

lobe is 27 dB lower than the main beam. The uniform facetted surface is obtained in GRASP by first defining a uniform triangular grid with side length s in the xy-plane of the global CS. The node points of this grid are assigned a z-value such that the points are located on the paraboloid reflector surface. Finally, the node points are connected with straight lines to form the planar triangular facets. The uniform facetted surface with s = 1250 mm is shown in.Figure 6.

It will be useful in the coming sections to express the nominal paraboloid not in the global CS but in the tilt CS depicted in Figure 3. This can be done in GRASP by using a surface defined by a second order polynomial. Similarly, the uniform triangular grid with side length s can be expressed in the xy-plane of the tilt CS. Still, the z-values of the node points of the grid are located on the paraboloid reflector surface.

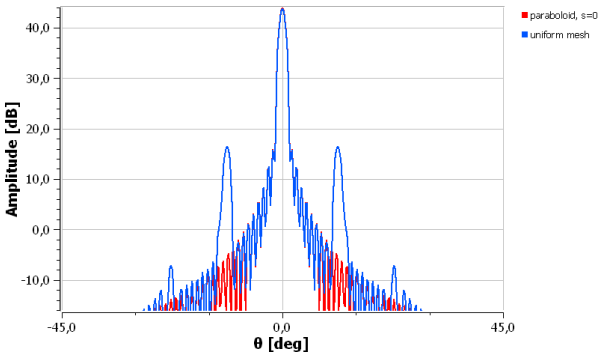

Figure 5. Co-polar radiation pattern in the φ = 90° cut. The red (blue) curve is obtained with the nominal (uniform mesh, side length s = 1250 mm) reflector.

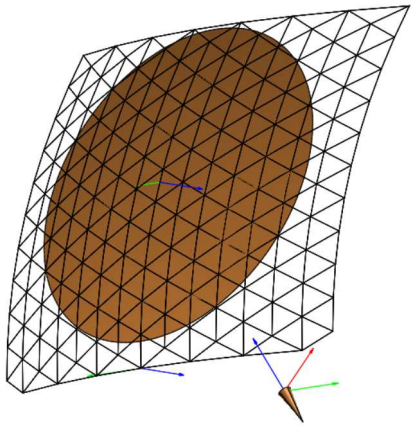

Figure 6. Uniform mesh in the global CS for the reflector defined in Figure 3 and triangular side length s = 1250 mm.

4. TECHNIQUES FOR GRATING LOBES REDUCTION

Several techniques for grating lobe reductions for LDR can be found in the literature. They all introduce a non-periodic arrangement of the triangular facets. A comparison of their performances is however not directly possible from the published results, since the authors use different aperture sizes, frequencies and mesh side lengths. In the coming sections we will focus on three possible techniques, and we will apply them to the antenna defined in Section 2, following the same approach described for the uniform mesh. This means that the z-values of the node points always lie on the paraboloid. The xy-node points of the meshes are generally defined in the global CS. For some meshes, the xy-node points will also be distributed in the tilt CS. This will be clearly stated in the text. A detailed comparison of the obtained results is given in Section 6 for a similar number N of nodes inside the reflector rim. All patterns are computed by GRASP.

4.1 Fibonacci distribution

The first non-uniform triangular mesh is the so-called Fibonacci mesh, described in [6]. This type of mesh is constructed in the following way: Let (x_k, y_k) indicate the point positions in the projected aperture plane, these point coordinates can be calculated as

$$x_k = R\sqrt{\frac{k}{N}}\cos\left(\frac{2\pi k}{\varphi^2}\right) + O_x \quad (3)$$

$$y_k = R\sqrt{\frac{k}{N}}\sin\left(\frac{2\pi k}{\varphi^2}\right) + O_y \quad (4)$$

where k is running from 1 to N (N being the number of grid points inside the rim), R = 6.5 m is the radius of the grid area (slightly larger than aperture radius = 6.0 m), $\varphi = \frac{1+\sqrt{5}}{2}$ and (O_x, O_y) = (7.5 m, 0 m) is the centre of the reflector. The mesh side length is determined by N. For the comparison of Section 6, N = 110 is considered. The corresponding node points in the global xy-plane are shown in Figure 7, and the amplitude of the co-polar field in the azimuth elevation grid is seen in Figure 8.

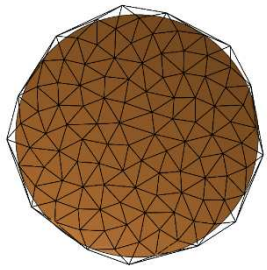

Figure 7. Fibonacci node points in the global xy-plane, with N = 110.

It can be observed that the symmetric and isolated grating lobes of Figure 4 have disappeared and have been replaced by a more rotationally symmetric distribution confined in the [0:12°] angular region. A cut through the φ=90° is shown in Figure 9, where in blue the uniform mesh result is shown as a reference.

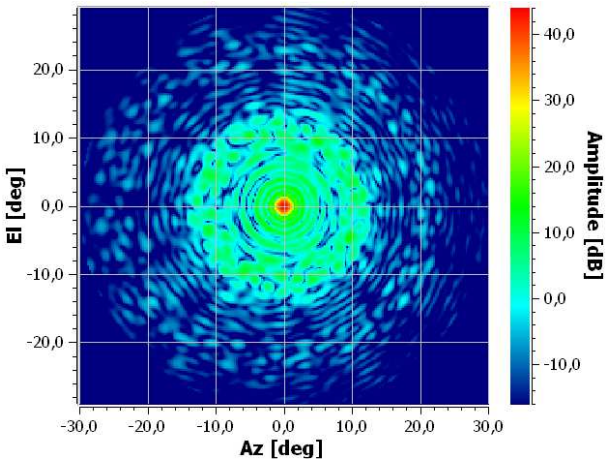

Figure 8. Co-polar radiation pattern for the Fibonacci mesh with $N = 110$.

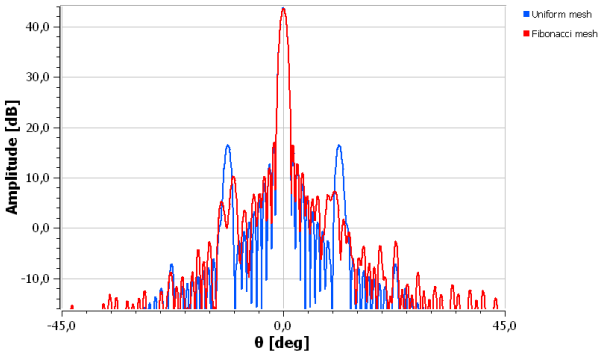

Figure 9. Co-polar radiation pattern in the φ = 90° cut. The red (blue) curve is for the Fibonacci mesh (uniform mesh, side length $s = 1250$ mm).

4.2 Penrose distribution

Zong et. al. [7] propose a Penrose-tiling-like configuration of the mesh in order to avoid symmetry and periodicity of the facets. Two triangular Penrose like meshes, kites and rhombi, containing a total of 91 and 86 nodes inside the reflector rim, respectively, are shown in Figure 10.

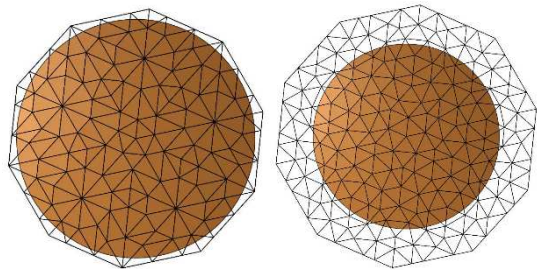

Figure 10. Penrose kites with $N = 91$ (left) and rhombi with $N = 86$ (right) node points in the global xy-plane.

It is seen that the kites distribution implies that nodes are connected to a variable number of neighboring nodes, making the mechanical realization challenging. The grid and cut plots for the Penrose rhombi mesh are given in Figure 11 and Figure 12. The Penrose kites distribution provides similar results.

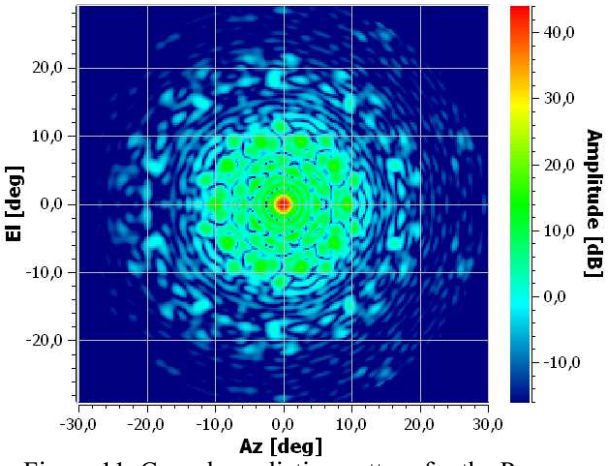

Figure 11. Co-polar radiation pattern for the Penrose rhombi mesh.

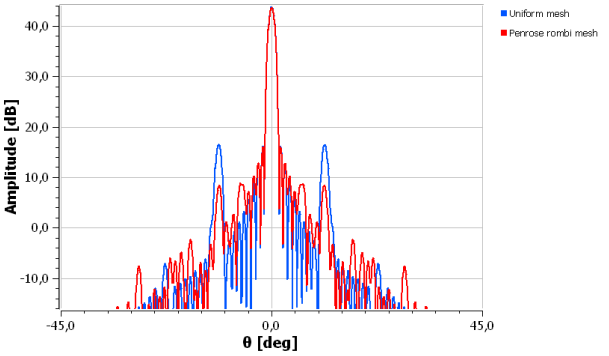

Figure 12. Co-polar radiation pattern in the φ = 90° cut. The red (blue) curve is for the Penrose rhombi mesh (uniform mesh, side length $s = 1250$ mm).

4.3 Arithmetic distribution

Following [8], a so-called arithmetic mesh can be constructed, see Figure 13. Along the six symmetry directions, the triangular side length is increased radially such that $L2/L1 = 2$. Consecutive side lengths differ by a constant that is in an arithmetic series, which means that the nth side length along each symmetric radial direction is:

$$Ln = L1\left[1 + \frac{n-1}{N}\right], n = 1, 2, \ldots, N + 1. \quad (5)$$

In the situation in Figure 13, $N = 5$. The arithmetic mesh generated with an average side length of 1250 mm is shown in Figure 14. Its co-polar radiation pattern in a spherical grid is seen in Figure 15. The six fold structural symmetry of the grating lobes is clearly visible, but comparing with the uniform mesh pattern of Figure 4 the grating lobes are smeared out. A cut through φ=90° is shown in Figure 16 in red, together with the field of the uniform mesh in blue.

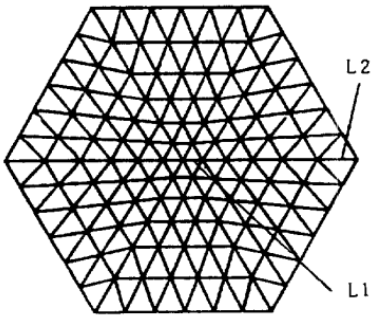

Figure 13. Arithmetic mesh described by [7].

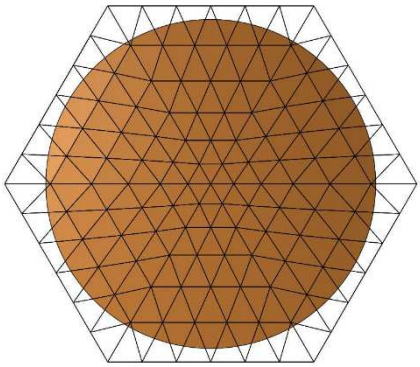

Figure 14. Arithmetic mesh in the global *xy*-plane with an average radial side length of 1250 mm, corresponding to L1 = 833.28 mm in Figure 13.

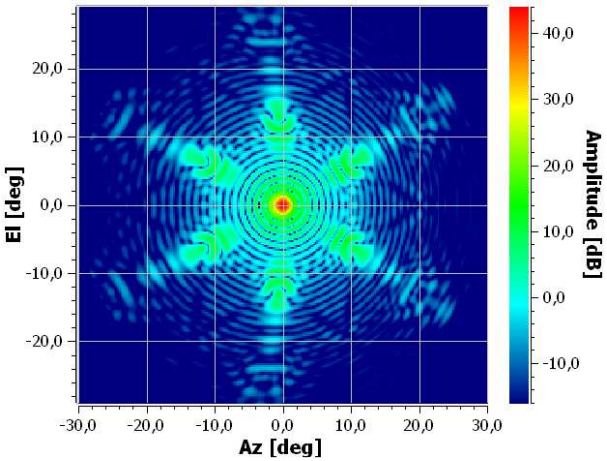

Figure 15. Co-polar radiation pattern for the arithmetic mesh with average side length s = 1250 mm.

The arithmetic mesh can also be obtained by placing the *xy*-node points not in the global, but in the tilt CS, see the distribution of Figure 17.

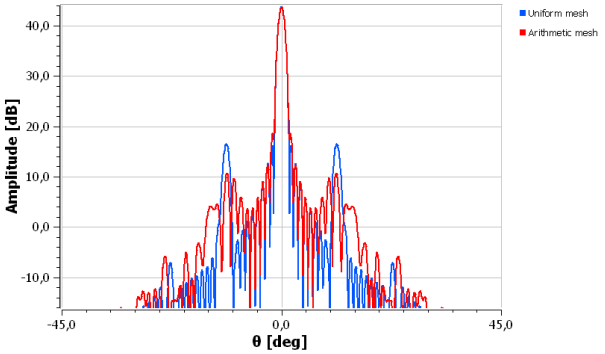

Figure 16. Co-polar radiation pattern in the φ = 90° cut. The red (blue) curve is for the arithmetic mesh (uniform mesh, side length s = 1250 mm).

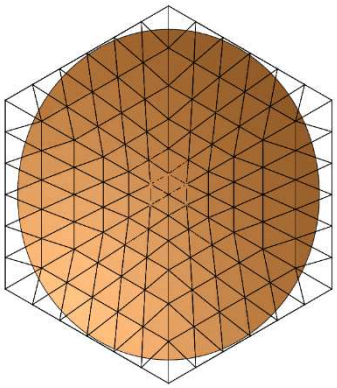

Figure 17. Arithmetic mesh in the tilt *xy*-plane with an average radial side length of 1250 mm, corresponding to L1 = 833.28 mm in Figure 13.

5. UNIFORM MESH SATISFYING EQUILIBRIUM OF FORCES

The uniform mesh described in Section 3 has been accurately modelled by LSS, in order to both consider a realistic rim of the reflector and satisfy the equilibrium of the forces at the mesh nodes. The mesh obtained with an average size length s =1176 mm is seen in Figure 18. It is noted that the *xy*-coordinates of the node points lie in the *xy*-plane of the tilt CS of Figure 3, and the *z*-coordinates are located on the paraboloid. From Figure 18 it is seen that the size of the triangles is not constant over the reflector, but a small increase in the mesh size is noticeable going from the center to the edge of the reflector. This behavior is similar to the one seen by the arithmetic mesh of Section 4.3, though here the ratio between the sizes is smaller than 2. The co-polar field of Figure 19 is very similar to Figure 4, while in Figure 20 we can observe a small decrease in the peak of the sidelobes, due to the slightly smaller mesh length used by LSS.

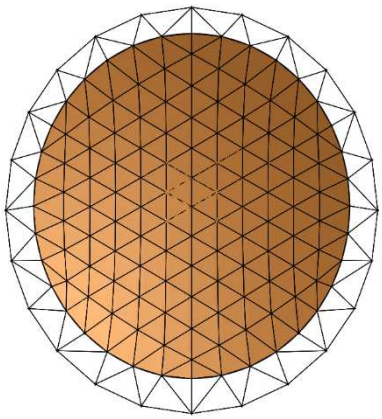

Figure 18. Uniform mesh provided by LSS in the tilt *xy*-plane with average side length of 1176 mm.

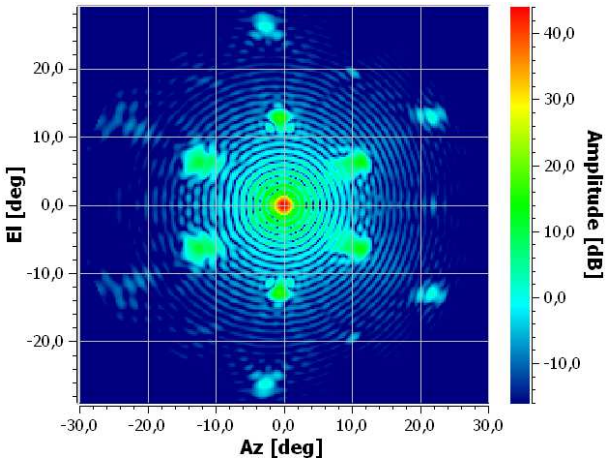

Figure 19. Co-polar radiation pattern for the uniform mesh from LSS with average side length s = 1176 mm.

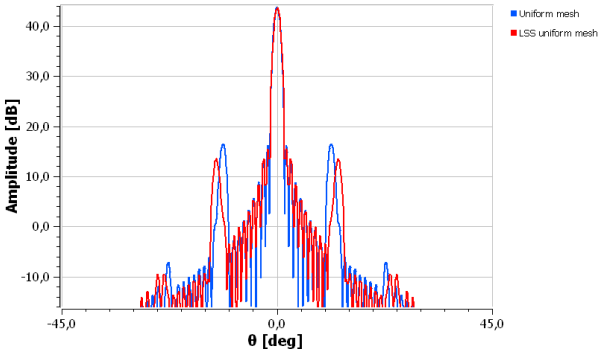

Figure 20. Co-polar radiation pattern in the φ = 90° cut. The red (blue) curve is for the uniform mesh of LSS (uniform mesh, side length s = 1250 mm).

6. COMPARISON OF GRATING LOBE REDUCTION TECHNIQUES

The meshes presented so far are mechanically similar since they have approximately the same number of nodes inside the reflector rim. In order to trade-off their performances in a systematic way, their azimuth and elevation grid patterns are subtracted in amplitude to the pattern of the nominal paraboloid, which does not show grating lobes, as seen in Figure 5. More specifically, we consider in the subtraction the envelope of the pattern of the nominal paraboloid, in order to disregard the nulls of the field. Finally, we extract the maximum difference, see last column of Table 1.

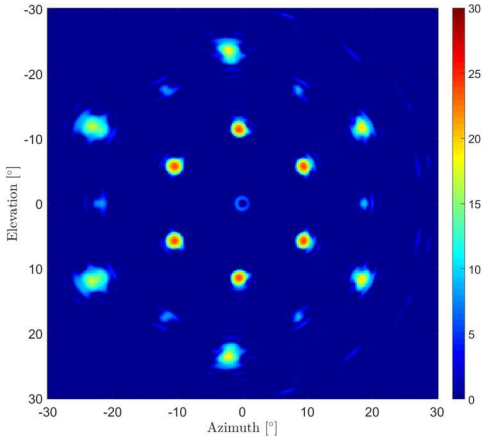

Figure 21. Uniform mesh: co-polar difference grid.

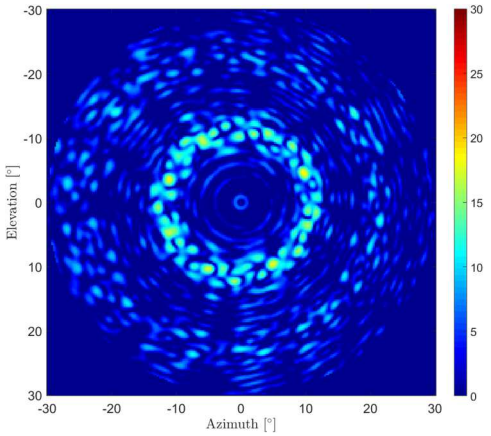

Figure 22. Fibonacci mesh: co-polar difference grid.

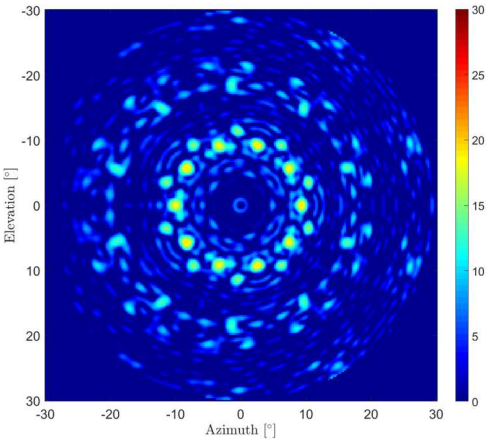

Figure 23. Penrose rhombi: co-polar difference grid.

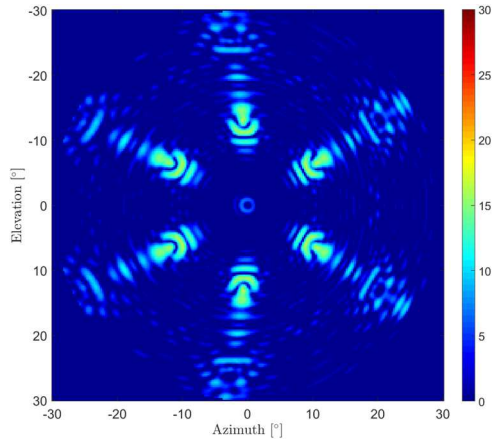

Figure 24. Arithmetic mesh: co-polar difference grid.

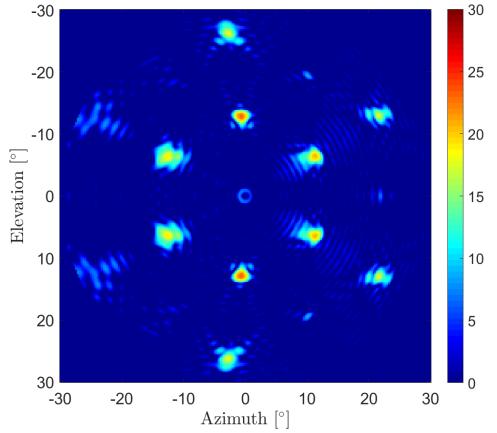

Figure 25. LSS uniform mesh: co-polar difference grid.

The maximum difference between the mesh patterns and the envelope curve of the pattern of the paraboloid is a measure for the grating lobe level. The smaller is the difference, the lower are the grating lobes generated by the mesh. Plots of this amplitude difference are given in the following figures. It is seen that the arithmetic mesh provides the lowest values of the difference, i.e. the lowest grating lobes and thus the best performances.

Finally, Figure 26 shows the patterns in the angular region around the main beam in the φ=0° plane. The field of the regular paraboloid is shown in black, together with the ones of the different meshes. It is seen that the uniform, Fibonacci and Penrose meshes provide a pattern that closely reproduces the one of the nominal paraboloid also in the first side lobe, besides a difference which is at maximum 0.44 dBi. The arithmetic mesh, both when described in the global and tilt CS (see red and light blue curves), introduces a clearly asymmetric first sidelobe, which is up to 3.6 dBi higher for positive theta relative to the sidelobe of the nominal paraboloid. A similar asymmetry, though less pronounced in peak, is given by the uniform mesh of LSS. The asymmetry in the first sidelobe in the φ=0° plane for negative theta is smaller in peak than the one observed for positive theta.

In the φ=90° plane the field is generally symmetric relative to θ=0°, as it should be, and the field from the uniform, Penrose rhombi and uniform LSS mesh coincide with the field of the nominal paraboloid. The arithmetic mesh generates a field that is symmetric relative to θ=0° but the first sidelobe is around 2.4 dBi higher than the one from the paraboloid, both when the global and tilt CS are used.

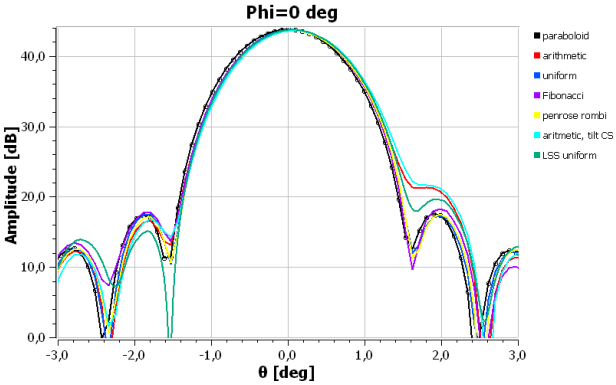

Figure 26. Comparison of the far-field amplitude pattern for the different mesh types, around the first sidelobe region, in φ =0° plane.

To better understand the origin of the asymmetry of the first side lobe, it is interesting to look at the phase distribution of the field reflected by the reflector on a plane parallel to the *xy*-plane of the cut CS, see Figure 27 where the results for the nominal paraboloid, the uniform mesh and the arithmetic mesh are shown in the same scale.

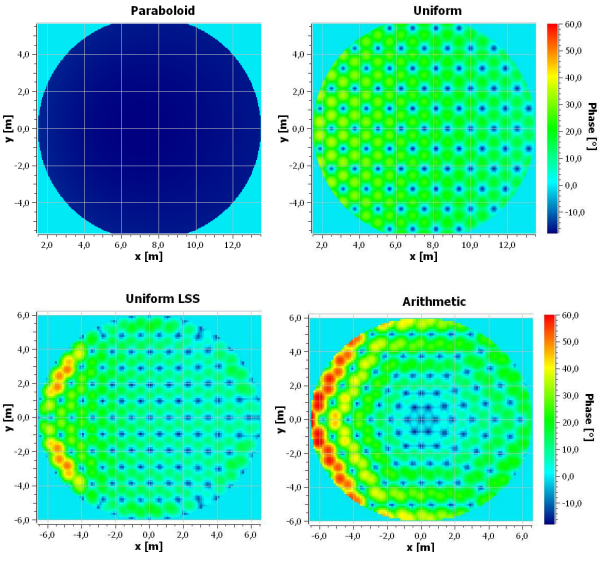

Figure 27. Phase plots in the cut CS *xy*-plane for the nominal paraboloid (top left), uniform mesh (top right), LSS uniform (bottom left) and arithmetic (bottom right).

It is clearly seen that the uniform phase distribution provided by the paraboloid is modified by the mesh surfaces which are constituted by planar triangles. While the same phase is provided at the node points which lie on the paraboloid (see the blue dots), phase variations are

visible for reflector points lying between the node points. In particular, a visible phase difference can be noted for the arithmetic mesh at the bottom of the reflector, i.e. close to the vertex of the paraboloid. This is where the paraboloid has the largest curvature, and this is also where the arithmetic mesh features the largest planar triangles. A similar, but weaker, behaviour is seen in the phase plot given by the uniform mesh provided by LSS, where larger triangles are also present where the curvature is larger. It seems therefore that a better control of the first sidelobe could be achieved by reducing the size of the planar triangles at the bottom of the reflector, in order to better fit the nominal paraboloid.
In Table 1 a summary of the mesh performances is given. The rms relative to the nominal paraboloid obtained by the different mesh reflectors is contained in the interval [9.8: 12.8] mm.

Table 1. Summary of performances for the nominal paraboloid and the different meshes.

Mesh type	Average mesh side length [mm]	Nodes inside rim	Peak directivity [dBi]	Maximum difference with paraboloid envelope [dBi]
Nominal	0	∞	43.85	-
Uniform	1250	85	43.74	23.88
Fibonacci	1307	93	43.68	18.91
Penrose, rhombi	1418	86	43.63	19.33
Arithmetic	1366	91	43.66	15.99
Uniform LSS	1176	120	43.72	23.15

7. CONCLUSIONS

A number of techniques for grating lobes reduction applicable to large deployable mesh reflectors have been investigated and applied to a 12 m offset reflector in L band. The arithmetic mesh provides the best performances, with a reduction of more than 7 dBi relative to the grating lobes provided by a traditional uniform mesh. Its drawback is an asymmetric first sidelobe, which is up to 3.6 dBi higher than the first sidelobe of a smooth paraboloid. This can possibly be improved by reducing the size of the planar triangles at the bottom of the reflector, in order to better fit the nominal paraboloid where the reflector curvature is largest.

8. REFERENCES

1. L. Datashvili, N. Maghaldadze, J. Pauw, S. Endler, H. Baier, L. Gigineishvili, “Advanced architectures of large space deployable mesh reflectors: from medium to very large sizes”, 2nd International Scientific Conference Advanced Lightweight Structures and Reflector Antennas, 1-3 October 2014, Tbilisi, Georgia.

2. L. Datashvili, “Deployable Space Reflector”, Georgian Patent Application ID: 12873/01, 19.10.2012

3. Mangenot, C., et al.: Large Antenna Working Group, ESA Final Report, TEC-EEA/2010.595/CM (2010).

4. Thomson, M. W., “The AstroMesh deployable reflector”, In IUTAM-IASS Symposium on Deployable Structures:Theory and Applications (Cambridge, UK, 6–9 September 1998), S. Pellegrino and S. D. Guest, Eds., Kluwer Academic Publishers, Dordrecht, The Netherlands, 2000, pp. 435–446.

5. P. B. Focardi, R. Y. Samii, “6-m mesh reflector antenna for SMAP: modeling the RF performance of a challenging Earth-orbiting instru-ment,” 2011 IEEE International Symposium on Antennas and Propagation, Spokane, pp. 2987-2990.

6. J.C. Angevain, G. Rodrigues, J. Santiago-Prowald, C. Mangenot, L. Datashvili, “Sidelobe level reduction of faceted mesh reflector antenna using phyllotactic arrangements”, 2nd International Scientific Conference Advanced Lightweight Structures and Reflector Antennas, 1-3 October 2014, Tbilisi, Georgia.

7. Y. Zong, B. Duan, Y. Ban, W. Wang, W. Xu, C. Wang, J.Du, “Surface configuration design of cable-network reflectors considering the radiation pattern”, IEEE Transactions on Antennas and Propagation, Vol.62, No.6, June 2014.

8. T. Orikasa, T. Obisui, T. Okamoto; “Sidelobe suppression of mesh reflector antenna by non-regular interval”, IEEE Antenna and Propagation International Symposium, 28 June - 2 July 1993, New York, USA.

9. L. Datashvili et al, Scalable Large Deployable Mesh Antenna Reflector Technology Demonstration, proceedings of the ECSSMET, 27-30 of September 2016, Toulouse France.